universe

MDPI

Article

A Comparison Study of Collisions at Relativistic Energies Involving Light Nuclei

Hai-Cheng Wang, Song-Jie Li, Jun Xu * and Zhong-Zhou Ren

School of Physics Science and Engineering, Tongji University, Shanghai 200092, China
* Correspondence: junxu@tongji.edu.cn

Abstract

We present extensive comparisons of ^{16}O+^{16}O collisions at a center-of-mass energy per nucleon pair $\sqrt{s_{NN}}$ = 200 GeV and ^{208}Pb+^{16}O collisions at $\sqrt{s_{NN}}$ = 68.5 GeV as well as ^{20}Ne+^{20}Ne collisions at $\sqrt{s_{NN}}$ = 200 GeV and ^{208}Pb+^{20}Ne collisions at $\sqrt{s_{NN}}$ = 68.5 GeV based on a multiphase transport (AMPT) model. We recommend measuring the ratio of the elliptic flow to the triangular flow, which shows appreciable sensitivity to the structure of light nuclei, as also found in other studies. This is especially so if the observable is measured near the target rapidity in ^{208}Pb+^{16}O or ^{208}Pb+^{20}Ne collisions , as originally found in the present study. Our study serves as a useful reference for understanding the effect of structure on observables in collisions involving light nuclei under analysis or on the schedule.

Keywords: relativistic heavy-ion collisions; transport model; anisotropic flow; nucleus deformation; light nuclei

check for updates

Academic Editor: Giuseppe Verde

Received: 7 August 2025
Revised: 26 August 2025
Accepted: 27 August 2025
Published: 1 September 2025

Citation: Wang, H.-C.; Li, S.-J.; Xu, J.; Ren, Z.-Z. A Comparison Study of Collisions at Relativistic Energies Involving Light Nuclei. *Universe* **2025**, *11*, 296. https://doi.org/10.3390/universe11090296

Correction Statement: This article has been republished with a minor change. The change does not affect the scientific content of the article and further details are available within the backmatter of the website version of this article.

Copyright: © 2025 by the authors. Licensee MDPI, Basel, Switzerland. This article is an open access article distributed under the terms and conditions of the Creative Commons Attribution (CC BY) license (https://creativecommons.org/licenses/by/4.0/).

1. Introduction

Understanding the structure of nuclei is a fundamental goal of nuclear physics. Besides traditional methods, relativistic heavy-ion collisions provide an alternative way of extracting the density distribution of colliding nuclei [1]. In the past few years, various probes for nucleus deformation have been proposed and applied in experimental analysis. The basic idea is that the deformation of colliding nuclei may enlarge the anisotropy of the overlap region and enhance the fluctuation of the overlap area in the initial stage of the collision, which will lead to larger anisotropic flows and stronger transverse momentum fluctuations in the final stage of the collision [2,3]. Using this principle, researchers have successfully extracted the deformation parameters of heavy nuclei such as ^{96}Ru [4], ^{96}Zr [4], ^{197}Au [5], and ^{238}U [6] as well as the shape of ^{129}Xe [7–9]. The focus of the community has now turned to collisions involving light nuclei [10–16], which have not only large deformations but also different α-cluster configurations. For example, ^{16}O may have a tetrahedral structure formed by four α clusters [17–19] with considerable octupole deformation, while ^{20}Ne may have a bowling-pin structure consisting of five α clusters [20,21] with considerable quadrupole and octupole deformation. The existence of α-cluster structure may break the scaling relation between the deformation parameter and specific observables in relativistic heavy-ion collisions, such as the anisotropic flows and the transverse momentum fluctuation [22]. While these observables are sensitive to the deformation of colliding nuclei, it is of interest to directly probe the existence of α-cluster structure in light nuclei through their collisions at relativistic energies [23]. On the experimental side, in addition to ^{16}O+^{16}O (light–light) collisions at the top energy of the Relativistic Heavy Ion Collider,

which are currently under analysis [24], the System for Measuring Overlap with Gas in the Large Hadron Collider beauty experiment enables the study of fixed-target collisions at relativistic energies, and collisions involving light nuclei such as ^{208}Pb+^{16}O and ^{208}Pb+^{20}Ne (heavy–light) collisions are scheduled for future experiments (see, e.g., Refs. [12,25–27]).

It is of interest to compare and understand the different effects of deformation and clustering in light–light collisions and heavy–light collisions on the collision dynamics and final observables. Compared to light–light collisions, heavy–light collisions are carried out at a lower center-of-mass collision energy but have a larger initial overlap area. The event-by-event fluctuation is expected to be stronger in light–light collisions than in heavy–light collisions. Therefore, different correspondence between initial anisotropies and final flows as well as between the initial overlap size and the final transverse momentum distribution may exist in light–light and heavy–light collisions. While it is difficult to probe directly the existence of α-cluster structure in light–light collisions through mid-rapidity observables [23], it is of interest to investigate whether this is the case in heavy–light collisions. Furthermore, in asymmetric systems such as heavy–light collisions, it remains to be determined at what rapidity observables are most sensitive to the structure of light nuclei. The above will be studied in the present paper based on the AMPT model. We will compare observables in light–light and heavy–light collisions by assuming light nuclei have a spherical shape, a deformed Woods–Saxon (WS) shape, or an α-cluster structure, in order to investigate the effects of deformation and α-cluster structure in different collision systems.

The rest of the paper is organized as follows. Section 2 gives the density distributions of ^{16}O and ^{20}Ne and briefly describes the framework of the AMPT model. Section 3 presents extensive comparisons of the initial anisotropies as well as final anisotropic flows and transverse momentum fluctuations for different collision systems and different initial configurations. We give a brief conclusion in Section 4.

2. Theoretical Framework

The density distributions of ^{16}O and ^{20}Ne are obtained based on a Bloch–Brink wave function approach, where empirical nucleon–nucleon interactions are used and the nucleon wave function inside each α cluster is approximated as a Gaussian form. It is assumed that four α clusters form a tetrahedron structure in ^{16}O and five α clusters form a bowling-pin structure in ^{20}Ne. The distance parameters in the corresponding α-cluster configurations are determined by minimizing the total energy after the angular-momentum projection of the whole wave function. For details of the framework in obtaining the wave functions and the density distributions in ^{16}O and ^{20}Ne, we refer the reader to Ref. [22].

Figures 1a and 1b display respectively the density contours of ^{16}O and ^{20}Ne with α-cluster structure obtained from the above framework. In order to distinguish the α-cluster effect from the deformation effect on final observables, we have also constructed density distributions of the deformed WS form for both ^{16}O and ^{20}Ne as follows:

$$\rho(r,\theta) = \frac{\rho_0}{1+\exp\left\{\frac{r-R_0[1+\beta_2 Y_{2,0}(\theta)+\beta_3 Y_{3,0}(\theta)]}{d}\right\}}. \quad (1)$$

In the above equation, ρ_0 is the normalization constant, R_0 is the radius parameter, d is the diffuseness parameter, β_2 and β_3 are the deformation parameters, and $Y_{2,0}$ and $Y_{3,0}$ are the spherical harmonics. The deformation parameters β_n are determined in such a way that the WS-form density distributions have the same intrinsic multipole moments

$$Q_n = \int \rho(\vec{r}) r^n Y_{n,0}(\theta) d^3r \quad (2)$$

as the density distributions $\rho(\vec{r})$ with α-cluster structure. R_0 and d are determined in such a way that the deformed WS distributions have the same RMS radii (characterized by $\langle r^2 \rangle$) and the same surface diffuseness (characterized by $\langle r^4 \rangle$) as the density distributions $\rho(\vec{r})$ with α-cluster structure, where the lth-order moment of r is defined as $\langle r^l \rangle = \int \rho(\vec{r}) r^l d^3r / \int \rho(\vec{r}) d^3r$. In this way, the density distributions of ^{16}O and ^{20}Ne with the above mentioned deformed WS form have the same global shape as the more realistic ones with α-cluster structure. The values of R_0, d, β_2, and β_3 in the WS-form density distributions for both ^{16}O and ^{20}Ne are listed in Table 1. It can be seen that the density distribution of ^{16}O has a considerable β_3, and that of ^{20}Ne has considerable β_2 and β_3, as intuitively expected. The resulting density contours for the deformed WS distributions are displayed in Figure 1c,d. In order to investigate separately the deformation effects of colliding nuclei on final observables, we have further considered the distributions of the spherical WS form by simply setting $\beta_n = 0$ in Equation (1). This way, the nucleus size is the same for the three cases, while the central density in the spherical WS form is higher than that from the spherical Skyrme–Hartree–Fock calculation [28].

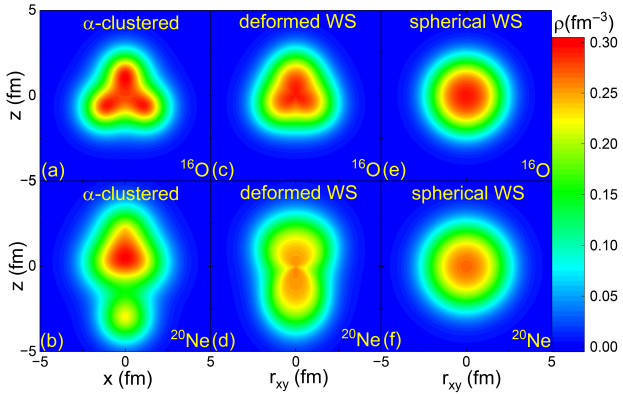


Figure 1. Density contours of ^{16}O and ^{20}Ne with α-cluster structure (**a**,**b**), of a deformed WS form (**c**,**d**), and of a spherical WS form (**e**,**f**). r_{xy} represents the radius in the x–o–y plane.

Table 1. Parameter values for the deformed WS density distributions of ^{16}O and ^{20}Ne.

	R_0 (fm)	d (fm)	β_2	β_3
^{16}O	1.973	0.507	0	0.223
^{20}Ne	2.160	0.580	0.666	0.250

To describe non-equilibrium dynamics in collisions involving light nuclei, transport models are favored over hydrodynamics models. We will compare ^{16}O+^{16}O collisions at $\sqrt{s_{NN}}$ = 200 GeV under experimental analysis and ^{208}Pb+^{16}O collisions at $\sqrt{s_{NN}}$ = 68.5 GeV on the schedule, as well as the hypothetical ^{20}Ne+^{20}Ne collisions at $\sqrt{s_{NN}}$ = 200 GeV and ^{208}Pb+^{20}Ne collisions at $\sqrt{s_{NN}}$ = 68.5 GeV on the schedule, based on the AMPT model. The density distribution of ^{208}Pb is set as the empirical spherical WS form in AMPT. The coordinates of participant nucleons in ^{16}O or ^{20}Ne are sampled according to the density distributions shown in Figure 1 with recentering and random orientations. In the string melting version of the AMPT model used in the present study, hadrons generated by the Heavy-Ion Jet Interacting Generator model [29] from collisions of participant nucleons are converted to partons according to the flavor and spin structures of their valence quarks. The momentum spectrum of these initial partons is described by the Lund string fragmentation function

$$f(z) \propto z^{-1}(1-z)^a \exp(-bm_\perp^2/z), \tag{3}$$

with z being the light-cone momentum fraction of the produced hadron of transverse mass $m_\perp$ with respect to that of the fragmenting string, while a and b are two parameters. We set a = 0.5 and b = 0.9 GeV^{-2} in the present study [30,31]. Sub-nucleon effects [32–42], which may affect the effective area of the nuclear overlap and the initial parton production, are not considered in the present study. The evolution of the partonic phase is described by Zhang's parton cascade model [43], including two-body elastic collisions with the differential cross section

$$\frac{d\sigma}{dt} \approx \frac{9\pi\alpha_s^2}{2(t-\mu^2)^2}, \tag{4}$$

where t is the standard Mandelstam variable for four-momentum transfer. In the present study, we set the strong coupling constant α_s to 0.33 and the screening mass μ to 3.2 fm^{-1}, corresponding to a parton scattering cross section of 1.5 mb [30,31]. After the kinetic freeze-out of these partons, a spatial coalescence model is used to combine quarks or antiquarks into hadrons according to their constituents. A relativistic transport model [44] including various elastic, inelastic, and decay channels is then used to describe the evolution of the hadronic phase until the kinetic freeze-out of all hadrons. For further details of the AMPT model, we refer the reader to Ref. [45]. Once the experimental data of, for example, the charged-particle multiplicity and the anisotropic flows in the corresponding collision systems are available, we can further calibrate the above mentioned parameters used in the AMPT model, which is beyond the scope of the present study.

3. Results and Discussion

In this section, we extensively compare observables in ^{16}O+^{16}O collisions at $\sqrt{s_{NN}}$ = 200 GeV and ^{208}Pb+^{16}O collisions at $\sqrt{s_{NN}}$ = 68.5 GeV with different initializations of ^{16}O, as well as ^{20}Ne+^{20}Ne collisions at $\sqrt{s_{NN}}$ = 200 GeV and ^{208}Pb+^{20}Ne collisions at $\sqrt{s_{NN}}$ = 68.5 GeV with different initializations of ^{20}Ne. We only compare results in central (0–10%) collisions with the maximum multiplicity and the maximum effect of structure, with the centrality determined by ordering the charged-particle multiplicities in all events.

We begin by comparing the spatial distributions of partons in the initial stage of different collision systems based on AMPT model calculations in Figure 2. Here, the nth-order anisotropic coefficient is calculated from

$$\epsilon_n = \frac{\sqrt{[\sum_i r_{\perp,i}^n \cos(n\phi_i)]^2 + [\sum_i r_{\perp,i}^n \sin(n\phi_i)]^2}}{\sum_i r_{\perp,i}^n}, \tag{5}$$

where $r_{\perp,i} = \sqrt{x_i^2 + y_i^2}$ and $\phi_i = \arctan(y_i/x_i)$, respectively, are the polar coordinate and the polar angle of the ith parton in the transverse plane. The fluctuation of the overlap's inverse area is defined as

$$\delta d_\perp^2 = (d_\perp - \langle d_\perp \rangle)^2, \tag{6}$$

where $d_\perp = 1/\sqrt{\overline{x^2}\;\overline{y^2}}$ is the overlap's inverse area [46], with $\overline{(...)}$ representing the average over all particles in one event, while $\langle ... \rangle$ represents the average over all events. A smaller number of initial partons and a smaller overlap area are observed in light–light than heavy–light collisions, and this leads to stronger fluctuations and thus systematically larger $\langle \epsilon_n \rangle$ and $\langle \delta d_\perp^2 \rangle$ in light–light collisions. In some cases, the anisotropic coefficients from light–light and heavy–light collision systems show the same sensitivity to the structure of light nuclei. $\langle \epsilon_3 \rangle$ in ^{16}O+^{16}O and ^{208}Pb+^{16}O collisions is rather insensitive to the octupole deformation of ^{16}O, owing to the similar contribution from fluctuations, but is enhanced by α-cluster structure in ^{16}O with a regular tetrahedron configuration. On the other hand, $\langle \epsilon_2 \rangle$ is more sensitive to the quadrupole deformation of colliding nuclei and is enhanced with deformed

or α-clustered ^{20}Ne in ^{20}Ne+^{20}Ne and ^{208}Pb+^{20}Ne collisions. However, $\langle\epsilon_n\rangle$ values do not necessarily show the same sensitivity to the density distribution of light nuclei in light–light and heavy–light collision systems. It can be seen that $\langle\epsilon_2\rangle$ generated from fluctuations in ^{16}O+^{16}O collisions is insensitive to the density distribution of ^{16}O, while the α-cluster structure in ^{16}O with a regular tetrahedron configuration slightly reduces fluctuations and thus $\langle\epsilon_2\rangle$ in ^{208}Pb+^{16}O collisions. $\langle\epsilon_3\rangle$ is insensitive to the density distribution of ^{20}Ne in ^{208}Pb+^{20}Ne collisions with more initial partons and larger overlap area, but it is enhanced with deformation or α-cluster structure in ^{20}Ne in ^{20}Ne+^{20}Ne collisions due to fewer initial partons and smaller initial overlap area. Consequently, the ratio $\langle\epsilon_2\rangle/\langle\epsilon_3\rangle$ is reduced with α-cluster structure in ^{16}O+^{16}O and ^{208}Pb+^{16}O collisions, and it is enhanced with deformed or α-clustered ^{20}Ne in ^{20}Ne+^{20}Ne and ^{208}Pb+^{20}Ne collisions. $\langle\delta d_\perp^2\rangle$ is insensitive to the density distribution of light nuclei in heavy–light collision systems due to the large overlap area, but it shows some sensitivity to the density distribution of light nuclei in light–light collision systems.

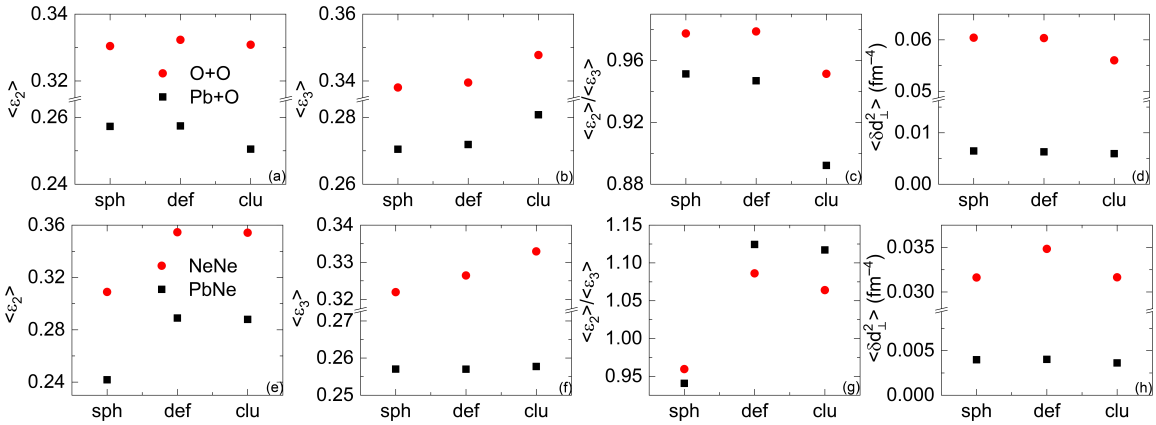


Figure 2. Comparison of the second-order anisotropic coefficient (**a**,**e**), the third-order anisotropic coefficient (**b**,**f**), their ratio (**c**,**g**), and the fluctuation of the overlap's inverse area (**d**,**h**) for initial partons in ^{16}O+^{16}O and ^{208}Pb+^{16}O collisions (upper) as well as in ^{20}Ne+^{20}Ne and ^{208}Pb+^{20}Ne collisions (lower) with the density distributions of ^{16}O and ^{20}Ne described by the spherical WS distribution (sph), by the deformed WS distribution (def), and by α-cluster structure (clu).

We now move to a comparison of the pseudorapidity distributions of the final charged particles in different collision systems shown in Figure 3. For the simplicity of the discussion, the pseudorapidity in the following results represents that in the laboratory frame, i.e., $\eta \sim \eta_{lab}$. It can be seen that the major multiplicity of charged particles is in the pseudorapidity range of $-1.5 < \eta < 1.5$ in light–light collisions, while it is in the pseudorapidity range of $4 < \eta < 7$ in heavy–light collisions, where a significantly higher peak is observed. Although there is no doubt that mid-rapidity observables are generally used as deformation probes of colliding nuclei in symmetric collision systems, it is challenging to choose the appropriate rapidity range for observables in asymmetric collision systems. For heavy–light collision systems, one expects that observables near target rapidities, e.g., $2 < \eta < 5$, will be more sensitive to the structure of target light nuclei. The multiplicity of charged particles is more sensitive to the density distribution of ^{20}Ne than to that of ^{16}O, likely due to the quadrupole deformation of ^{20}Ne, but this is not adequate to probe the deformation of ^{20}Ne in experimental analysis.

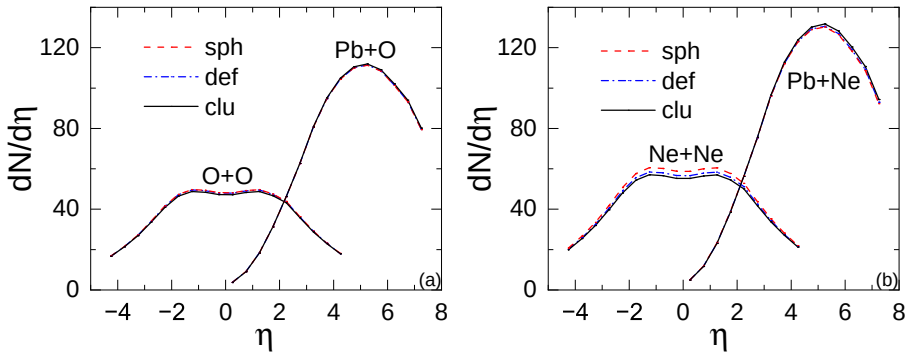


Figure 3. Comparison of final charged-particle pseudorapidity distributions in ^{16}O+^{16}O and ^{208}Pb+^{16}O collisions (**a**) as well as in ^{20}Ne+^{20}Ne and ^{208}Pb+^{20}Ne collisions (**b**) with the density distributions of ^{16}O and ^{20}Ne described by the spherical WS distribution (sph), by the deformed WS distribution (def), and by α-cluster structure (clu).

We then extensively compare the pseudorapidity distributions of final-state observables such as the elliptic flow $\langle v_2^2 \rangle$, the triangular flow $\langle v_3^2 \rangle$, and the transverse momentum fluctuation $\langle \delta p_T^2 \rangle$ in light–light and heavy–light collisions for different initial density distributions of light nuclei, and they are calculated according to

$$\langle v_n^2 \rangle = \langle \cos[n(\varphi_i - \varphi_j)] \rangle_{i,j}, \quad (7)$$

$$\langle \delta p_T^2 \rangle = \langle (p_{T,i} - \langle \overline{p_T} \rangle)(p_{T,j} - \langle \overline{p_T} \rangle) \rangle_{i,j}. \quad (8)$$

Here, $\langle ... \rangle_{i,j}$ represents the average over all possible combinations of i, j for all events, while $p_{T,i} = \sqrt{p_{x,i}^2 + p_{y,i}^2}$ and $\varphi_i = \arctan(p_{y,i}/p_{x,i})$, respectively, are the momentum and its polar angle for the ith particle in the transverse plane. To calculate $\langle v_n^2 \rangle$ and $\langle \delta p_T^2 \rangle$ at a certain pseudorapidity η, particles i and j are chosen from the range of $(\eta - 1.5, \eta + 1.5)$ with a gap of $|\Delta\eta| > 1$. Figure 4 compares the results in ^{16}O+^{16}O and ^{208}Pb+^{16}O collisions, and Figure 5 compares the results in ^{20}Ne+^{20}Ne and ^{208}Pb+^{20}Ne collisions. While in most cases $\langle v_2^2 \rangle$, $\langle v_3^2 \rangle$, and $\langle \delta p_T^2 \rangle$, respectively, are strongly correlated with $\langle \epsilon_2 \rangle$, $\langle \epsilon_3 \rangle$, and $\langle \delta d_\perp^2 \rangle$ as shown in Figure 2, the detailed behavior depends on the pseudorapidity range and other effects such as particle multiplicities, non-flow, etc. In Figure 4, the similar $\langle v_2^2 \rangle$ for different cases in ^{16}O+^{16}O collisions and the smaller $\langle v_2^2 \rangle$ with α-cluster structure in ^{208}Pb+^{16}O collisions are consistent with the behaviors of the corresponding $\langle \epsilon_2 \rangle$ shown in Figure 2a. The relative difference in $\langle v_3^2 \rangle$ from different initializations of ^{16}O depends on the pseudorapidity and is generally difficult to distinguish from the statistical error. $\langle \delta p_T^2 \rangle$ shows no sensitivity to the initialization of ^{16}O in either ^{16}O+^{16}O or ^{208}Pb+^{16}O collisions. In Figure 5, the larger $\langle v_2^2 \rangle$ values from deformed or α-clustered ^{20}Ne in both ^{20}Ne+^{20}Ne and ^{208}Pb+^{20}Ne collisions are consistent with the behaviors of the corresponding $\langle \epsilon_2 \rangle$ shown in Figure 2e. Compared to the spherical case, $\langle v_3^2 \rangle$ slightly decreases after incorporating the deformation or α-cluster structure in ^{20}Ne in both ^{208}Pb+^{20}Ne and ^{20}Ne+^{20}Ne collisions, in contrast to the relative difference in $\langle \epsilon_3 \rangle$ for different scenarios shown in Figure 2f. This is due to the effect of the quadrupole deformation of ^{20}Ne, which may reduce the triangular flow based on AMPT simulations as shown in Figure 3 (d) of Ref. [22]. Except that $\langle \delta p_T^2 \rangle$ is slightly smaller with spherical ^{20}Ne in ^{20}Ne+^{20}Ne collisions, $\langle \delta p_T^2 \rangle$ shows almost no sensitivity to the initialization of ^{20}Ne in either ^{20}Ne+^{20}Ne or ^{208}Pb+^{20}Ne collisions.

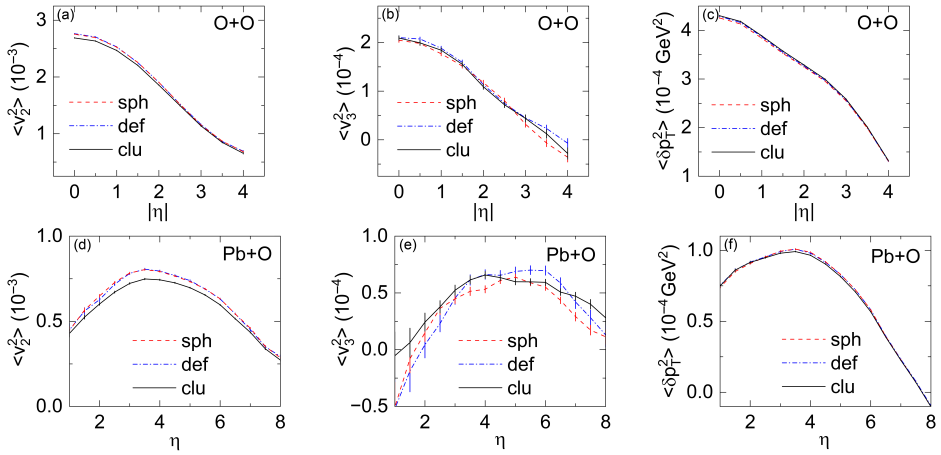


Figure 4. Comparison of pseudorapidity distributions of the elliptic flow (**a**,**b**), the triangular flow (**c**,**d**), and the transverse momentum fluctuation (**e**,**f**) in ^{16}O+^{16}O collisions (upper) and ^{208}Pb+^{16}O collisions (lower) with the density distributions of ^{16}O described by the spherical WS distribution (sph), by the deformed WS distribution (def), and by α-cluster structure (clu).

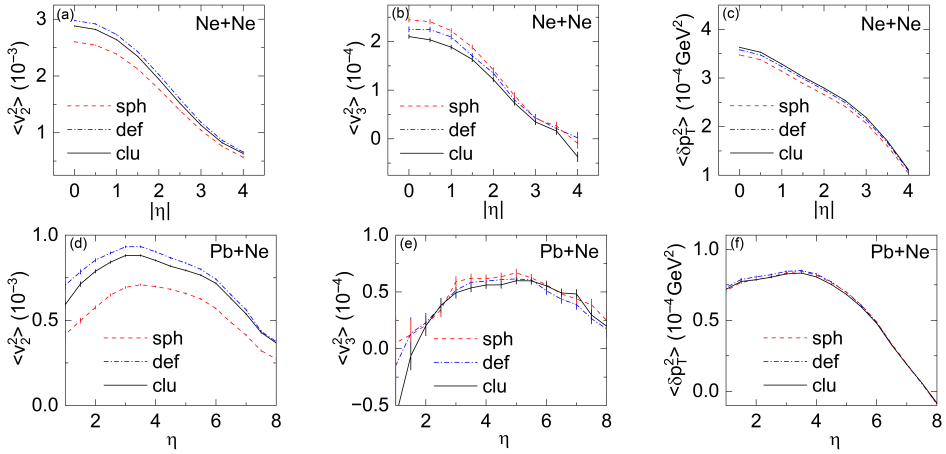


Figure 5. Comparison of pseudorapidity distributions of the elliptic flow (**a**,**b**), the triangular flow (**c**,**d**), and the transverse momentum fluctuation (**e**,**f**) in ^{20}Ne+^{20}Ne collisions (upper) and ^{208}Pb+^{20}Ne collisions (lower) with the density distributions of ^{20}Ne described by the spherical WS distribution (sph), by the deformed WS distribution (def), and by α-cluster structure (clu).

Let us now focus on observables in typical pseudorapidity ranges; the results are shown in Figure 6. For light–light collisions, we focus on the pseudorapidity range with the largest multiplicity of final charged particles, i.e., $-1.5 < \eta < 1.5$. For heavy–light collisions, we focus on the pseudorapidity range with the largest multiplicity of final charged particles, i.e., $4 < \eta < 7$, and the range near target rapidities, i.e., $2 < \eta < 5$, at which we expect that the results could be more sensitive to the structure of target light nuclei. Systematically, light–light collisions have stronger anisotropic flows and transverse momentum fluctuations than heavy–light collisions. The behaviors of $\langle v_2^2 \rangle$ are roughly similar to those of $\langle \epsilon_2^2 \rangle$ as shown in Figure 2a,e, while the relative $\langle v_3^2 \rangle$ from different initializations of light nuclei are different compared to those in Figure 2b,f. This shows that the elliptic flow manifests the initial geometry more clearly, while the triangular flow can be affected by other effects in dynamics of collisions involving light nuclei. Taking the ratios of the elliptic flow to the triangular flow in different collision systems reveals interesting behaviors: while $\langle v_2 \rangle / \langle v_3 \rangle$ shows almost no sensitivity to the structure of ^{16}O in the pseudorapidity range with the largest particle multiplicity in both ^{16}O+^{16}O and ^{208}Pb+^{16}O collisions, it shows appreciable sensitivity to the structure of ^{16}O near target rapidities in ^{208}Pb+^{16}O collisions, with the spherical case giving the largest $\langle v_2 \rangle / \langle v_3 \rangle$ and the deformation or α-clustered ^{16}O

leading to smaller $\langle v_2 \rangle / \langle v_3 \rangle$. On the other hand, $\langle v_2 \rangle / \langle v_3 \rangle$ is enhanced by deformation or α-cluster structure in ^{20}Ne in both ^{20}Ne+^{20}Ne and ^{208}Pb+^{20}Ne collisions, and the effect is stronger near target rapidities in ^{208}Pb+^{20}Ne collisions. We note that the centrality dependence of $\langle v_2 \rangle / \langle v_3 \rangle$ has also been shown to be sensitive to the α-cluster structure of ^{16}O in ^{16}O+^{16}O collisions in Refs. [13,47]. The transverse momentum fluctuation shows no sensitivity to the initialization of light nuclei. It can be seen that these observables are mainly sensitive to the global shape of light nuclei, while it is difficult to distinguish directly the density distribution of light nuclei with and without α-cluster structure in both light–light and heavy–light collisions, since the detailed α-cluster structure in light nuclei is mostly obscured by complicated dynamics in the partonic and hadronic phase.

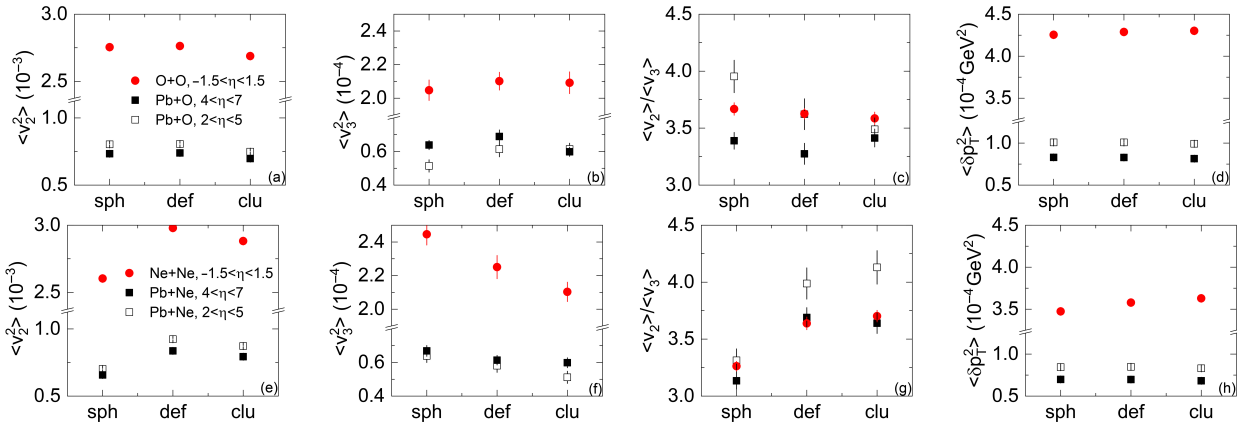


Figure 6. Comparison of the elliptic flow (**a**,**e**), the triangular flow (**b**,**f**), their ratio (**c**,**g**), and the transverse momentum fluctuation (**d**,**h**) in ^{16}O+^{16}O and ^{208}Pb+^{16}O collisions (upper) as well as in ^{20}Ne+^{20}Ne and ^{208}Pb+^{20}Ne collisions (lower) with the density distributions of ^{16}O and ^{20}Ne described by the spherical WS distribution (sph), by the deformed WS distribution (def), and by α-cluster structure (clu). Results for light–light collisions are calculated at mid-pseudorapidities ($-1.5 < \eta < 1.5$), and results for heavy–light collisions are calculated at different forward pseudorapidities ($2 < \eta < 5$ and $4 < \eta < 7$).

4. Summary

We present extensive comparisons of ^{16}O+^{16}O collisions at $\sqrt{s_{NN}}$ = 200 GeV and ^{208}Pb+^{16}O collisions at $\sqrt{s_{NN}}$ = 68.5 GeV as well as ^{20}Ne+^{20}Ne collisions at $\sqrt{s_{NN}}$ = 200 GeV and ^{208}Pb+^{20}Ne collisions at $\sqrt{s_{NN}}$ = 68.5 GeV based on the AMPT model; the main focus is on the sensitivity of observables to the structure of light nuclei. Light–light collisions systematically produce stronger anisotropic flows and transverse momentum fluctuations than heavy–light collisions. We found that the ratio of the elliptic flow to the triangular flow is a good probe of the structure of light nuclei as also mentioned in other studies, while the transverse momentum fluctuation shows weak sensitivity. In heavy–light collisions, observables near the target rapidity show stronger sensitivity to the structure of target light nuclei, as found for the first time in the present study. Observables are generally only sensitive to the global shape of colliding nuclei in both light–light and heavy–light collisions, while the detailed α-cluster structure in light nuclei cannot be distinguished from the constructed deformed Woods–Saxon shape after the complicated dynamics. Our study serves as a useful reference for understanding the structure effect on observables in collisions involving light nuclei under analysis or on the schedule.

Author Contributions: Conceptualization, H.-C.W., S.-J.L., J.X. and Z.-Z.R.; methodology, H.-C.W. and J.X.; software, H.-C.W.; validation, H.-C.W. and J.X.; formal analysis, H.-C.W. and S.-J.L.; investigation, H.-C.W., S.-J.L., J.X. and Z.-Z.R.; resources, J.X. and Z.-Z.R.; data curation, H.-C.W.; writing—original draft preparation, J.X.; writing—review and editing, H.-C.W. and J.X.; visualization,

H.-C.W. and J.X.; supervision, J.X. and Z.-Z.R.; project administration, J.X. and Z.-Z.R.; funding acquisition, J.X. and Z.-Z.R. All authors have read and agreed to the published version of the manuscript.

Funding: This work is supported by the National Key Research and Development Program of China under Grant No. 2023YFA1606701; by the National Natural Science Foundation of China under Grant Nos. 12375125, 12035011, and 11975167; and by the Fundamental Research Funds for the Central Universities.

Data Availability Statement: The raw data supporting the conclusions of this article will be made available by the authors on request.

Conflicts of Interest: The authors declare no conflicts of interest.

References

1. Jia, J.; Giacalone, G.; Bally, B.; Brandenburg, J.D.; Heinz, U.; Huang, S.; Lee, D.; Lee, Y.J.; Loizides, C.; Li, W.; et al. Imaging the initial condition of heavy-ion collisions and nuclear structure across the nuclide chart. *Nucl. Sci. Tech.* **2024**, *35*, 220. [CrossRef]
2. Jia, J. Shape of atomic nuclei in heavy ion collisions. *Phys. Rev. C* **2022**, *105*, 014905. [CrossRef]
3. Jia, J. Probing triaxial deformation of atomic nuclei in high-energy heavy ion collisions. *Phys. Rev. C* **2022**, *105*, 044905. [CrossRef]
4. Zhang, C.; Jia, J. Evidence of Quadrupole and Octupole Deformations in Zr96+Zr96 and Ru96+Ru96 Collisions at Ultrarelativistic Energies. *Phys. Rev. Lett.* **2022**, *128*, 022301. [CrossRef]
5. Giacalone, G.; Jia, J.; Zhang, C. Impact of Nuclear Deformation on Relativistic Heavy-Ion Collisions: Assessing Consistency in Nuclear Physics across Energy Scales. *Phys. Rev. Lett.* **2021**, *127*, 242301. [CrossRef]
6. Abdulhamid, M.I. et al. [STAR Collaboration] Imaging shapes of atomic nuclei in high-energy nuclear collisions. *Nature* **2024**, *635*, 67–72. [CrossRef]
7. Bally, B.; Bender, M.; Giacalone, G.; Somà, V. Evidence of the triaxial structure of ^{129}Xe at the Large Hadron Collider. *Phys. Rev. Lett.* **2022**, *128*, 082301. [CrossRef]
8. Aad, G.; Abbott, B.; Abbott, D.C.; Abeling, K.; Abidi, S.H.; Aboulhorma, A.; Abramowicz, H.; Abreu, H.; Abulaiti, Y.; Hoffman, A.C.A.; et al. Correlations between flow and transverse momentum in Xe+Xe and Pb+Pb collisions at the LHC with the ATLAS detector: A probe of the heavy-ion initial state and nuclear deformation. *Phys. Rev. C* **2023**, *107*, 054910. [CrossRef]
9. Acharya, S.; Agarwal, A.; AglieriRinella, G.; Aglietta, L.; Agnello, M.; Agrawal, N.; Ahammed, Z.; Ahmad, S.; Ahn, S.U.; Ahuja, I.; et al. Exploring nuclear structure with multiparticle azimuthal correlations at the LHC. arXiv:2409.04343. [CrossRef]
10. Wang, Y.; Zhao, S.; Cao, B.; Xu, H.j.; Song, H. Exploring the compactness of α clusters in O16 nuclei with relativistic O16+O16 collisions. *Phys. Rev. C* **2024**, *109*, L051904. [CrossRef]
11. Giacalone, G.; Bally, B.; Nijs, G.; Shen, S.; Duguet, T.; Ebran, J.P.; Elhatisari, S.; Frosini, M.; Lahde, T.A.; Lee, D.; et al. The unexpected uses of a bowling pin: Exploiting ^{20}Ne isotopes for precision characterizations of collectivity in small systems. arXiv:2402.05995.
12. Giacalone, G.; Zhao, W.; Bally, B.; Shen, S.; Duguet, T.; Ebran, J.P.; Elhatisari, S.; Frosini, M.; Lahde, T.A.; Lee, D.; et al. Anisotropic Flow in Fixed-Target Pb208+Ne20 Collisions as a Probe of Quark-Gluon Plasma. *Phys. Rev. Lett.* **2025**, *134*, 082301. [CrossRef]
13. Prasad, S.; Mallick, N.; Sahoo, R.; Barnaföldi, G.G. Anisotropic flow fluctuation as a possible signature of clustered nuclear geometry in O–O collisions at the Large Hadron Collider. *Phys. Lett. B* **2025**, *860*, 139145. [CrossRef]
14. Lu, Z.; Zhao, M.; Nielsen, E.G.D.; Li, X.; Zhou, Y. Signature of the α-clustering structure of Light Nuclei in Relativistic Nuclear Collisions. arXiv:2501.14852.
15. Zhao, X.L.; Ma, G.L.; Zhou, Y.; Lin, Z.W.; Zhang, C. Nuclear cluster structure effect in ^{16}O+^{16}O collisions at the top RHIC energy. arXiv:2404.09780.
16. Zhang, C.; Chen, J.; Giacalone, G.; Huang, S.; Jia, J.; Ma, Y.G. Ab-initio nucleon-nucleon correlations and their impact on high energy 16O+16O collisions. *Phys. Lett. B* **2025**, *862*, 139322. [CrossRef]
17. Freer, M.; Horiuchi, H.; Kanada-En'yo, Y.; Lee, D.; Meißner, U.G. Microscopic Clustering in Light Nuclei. *Rev. Mod. Phys.* **2018**, *90*, 035004. [CrossRef]
18. Bijker, R.; Iachello, F. Cluster structure of light nuclei. *Prog. Part. Nucl. Phys.* **2020**, *110*, 103735. [CrossRef]
19. Tohsaki, A.; Horiuchi, H.; Schuck, P.; Roepke, G. Status of α-particle condensate structure of the Hoyle state. *Rev. Mod. Phys.* **2017**, *89*, 011002. [CrossRef]
20. Zhou, B.; Funaki, Y.; Horiuchi, H.; Ma, Y.G.; Röpke, G.; Schuck, P.; Tohsaki, A.; Yamada, T. The 5α condensate state in ^{20}Ne. *Nature Commun.* **2023**, *14*, 8206. [CrossRef]
21. Röpke, G.; Xu, C.; Zhou, B.; Ren, Z.Z.; Funaki, Y.; Horiuchi, H.; Lyu, M.; Tohsaki, A.; Yamada, T. Alpha-like correlations in Ne, comparison of quartetting wave function and THSR approaches. *Eur. Phys. J. A* **2024**, *60*, 89. [CrossRef]

22. Wang, H.C.; Li, S.J.; Liu, L.M.; Xu, J.; Ren, Z.Z. Deformation probes for light nuclei in their collisions at relativistic energies. *Phys. Rev. C* **2024**, *110*, 034909. [CrossRef]
23. Liu, L.M.; Wang, H.C.; Li, S.J.; Zhang, C.; Xu, J.; Ren, Z.Z.; Jia, J.; Huang, X.G. Directly probing existence of α-cluster structure in Ne20 by relativistic heavy-ion collisions. *Phys. Rev. C* **2025**, *111*, L021901. [CrossRef]
24. Huang, S. Measurements of azimuthal anisotropies in ^{16}O+^{16}O and γ+Au collisions from STAR. arXiv:2312.12167.
25. Mariani, S. Fixed-Target Physics with the LHCb Experiment at CERN. Ph.D. Thesis, University of Florence, Florence, Italy, 1 December 2021.
26. Aaij, R.; Abdelmotteleb, A.S.W.; Beteta, C.A.; Abudinen, F.; Ackernley, T.; Adeva, B.; Adinolfi, M.; Afsharnia, H.; Agapopoulou, C.; Aidala, C.A.; et al. J/ψ and D^0 production in $\sqrt{s_{\rm NN}}$ = 68.5 GeV PbNe collisions. *Eur. Phys. J. C* **2023**, *83*, 658. [CrossRef]
27. Aaij, R. et al. [LHCb Collaboration] Centrality determination in heavy-ion collisions with the LHCb detector. *J. Instrum.* **2022**, *17*, P05009. [CrossRef]
28. Liu, L.M.; Li, S.J.; Wang, Z.; Xu, J.; Ren, Z.Z.; Huang, X.G. Probing configuration of α clusters with spectator particles in relativistic heavy-ion collisions. *Phys. Lett. B* **2024**, *854*, 138724. [CrossRef]
29. Wang, X.N.; Gyulassy, M. HIJING: A Monte Carlo model for multiple jet production in p p, p A and A A collisions. *Phys. Rev. D* **1991**, *44*, 3501–3516. [CrossRef]
30. Xu, J.; Ko, C.M. Pb-Pb collisions at $\sqrt{s_{NN}}$ = 2.76 TeV in a multiphase transport model. *Phys. Rev. C* **2011**, *83*, 034904. [CrossRef]
31. Xu, J.; Ko, C.M. Triangular flow in heavy ion collisions in a multiphase transport model. *Phys. Rev. C* **2011**, *84*, 014903. [CrossRef]
32. Mäntysaari, H.; Schenke, B.; Shen, C.; Tribedy, P. Imprints of fluctuating proton shapes on flow in proton-lead collisions at the LHC. *Phys. Lett. B* **2017**, *772*, 681–686. [CrossRef]
33. Welsh, K.; Singer, J.; Heinz, U.W. Initial state fluctuations in collisions between light and heavy ions. *Phys. Rev. C* **2016**, *94*, 024919. [CrossRef]
34. Schenke, B.; Venugopalan, R. Eccentric protons? Sensitivity of flow to system size and shape in p + p, p + Pb and Pb + Pb collisions. *Phys. Rev. Lett.* **2014**, *113*, 102301. [CrossRef]
35. Zheng, L.; Zhang, G.H.; Liu, Y.F.; Lin, Z.W.; Shou, Q.Y.; Yin, Z.B. Investigating high energy proton proton collisions with a multi-phase transport model approach based on PYTHIA8 initial conditions. *Eur. Phys. J. C* **2021**, *81*, 755. [CrossRef]
36. Zhao, X.L.; Lin, Z.W.; Zheng, L.; Ma, G.L. A transport model study of multiparticle cumulants in p + p collisions at 13 TeV. *Phys. Lett. B* **2023**, *839*, 137799. [CrossRef]
37. Wang, Q.; Pang, L.G.; Wang, X.N. Impact of Initial-State Nuclear and Sub-Nucleon Structures on Ultra-Central Puzzle in Heavy Ion Collisions. arXiv:2504.19208.
38. Wang, H.C.; Li, S.J.; Xu, J.; Ren, Z.Z. Disentangling effects of nucleon size and nucleus structure in relativistic heavy-ion collisions. *Phys. Lett. B* **2025**, *866*, 139516. [CrossRef]
39. Giacalone, G.; Schenke, B.; Shen, C. Constraining the Nucleon Size with Relativistic Nuclear Collisions. *Phys. Rev. Lett.* **2022**, *128*, 042301. [CrossRef]
40. Alvioli, M.; Strikman, M. Color fluctuation effects in proton-nucleus collisions. *Phys. Lett. B* **2013**, *722*, 347–354. [CrossRef]
41. Uzhinsky, V.; Galoyan, A. Gribov's inelastic screening in high energy nucleus-nucleus interaction. *Phys. Lett. B* **2013**, *721*, 68–73. [CrossRef]
42. Alvioli, M.; Frankfurt, L.; Perepelitsa, D.; Strikman, M. Global analysis of color fluctuation effects in proton– and deuteron–nucleus collisions at RHIC and the LHC. *Phys. Rev. D* **2018**, *98*, 071502. [CrossRef]
43. Zhang, B. ZPC 1.0.1: A Parton cascade for ultrarelativistic heavy ion collisions. *Comput. Phys. Commun.* **1998**, *109*, 193–206. [CrossRef]
44. Li, B.A.; Ko, C.M. Formation of superdense hadronic matter in high-energy heavy ion collisions. *Phys. Rev. C* **1995**, *52*, 2037–2063. [CrossRef]
45. Lin, Z.W.; Ko, C.M.; Li, B.A.; Zhang, B.; Pal, S. A Multi-phase transport model for relativistic heavy ion collisions. *Phys. Rev. C* **2005**, *72*, 064901. [CrossRef]
46. Schenke, B.; Shen, C.; Teaney, D. Transverse momentum fluctuations and their correlation with elliptic flow in nuclear collisions. *Phys. Rev. C* **2020**, *102*, 034905. [CrossRef]
47. Hu, J.Y.; Xu, H.j.; Wang, X.; Pu, S. Probing the tetrahedral α clusters in relativistic ^{16}O + ^{16}O collisions. arXiv:2507.01493.

Disclaimer/Publisher's Note: The statements, opinions and data contained in all publications are solely those of the individual author(s) and contributor(s) and not of MDPI and/or the editor(s). MDPI and/or the editor(s) disclaim responsibility for any injury to people or property resulting from any ideas, methods, instructions or products referred to in the content.